Fourier-transform terahertz near-field imaging of one-dimensional slit arrays: mapping of electric-field-, magnetic-field-, and Poynting vectors

M. A. Seo[1], A. J. L. Adam[2], J. H. Kang[3], J. W. Lee[1], S. C. Jeoung[4], Q. H. Park[3], P. C. M. Planken[2]*, and D. S. Kim[1]*

[1]School of Physics and Astronomy, Seoul National University, Seoul 151-747, Korea
[2]Faculty of Applied Sciences, Delft University of Technology, Lorentzweg 1, 2628 CJ Delft, The Netherlands
[3] Department of Physics, Korea University, Seoul 136-701, Korea
[4]Optical Nano Metrology Group, Korea Research Institute of Standard and Science, Daejeon 305-304, Korea
*Corresponding author: P.C.M.Planken@tudelft.nl and dsk@phya.snu.ac.kr
*DSK and PCMP's groups contributed equally to this work.

Abstract: We present 2D measurements of the full THz electric field behind a sample consisting of multiple slits in a metal foil. Our measurements, which have a sub-wavelength spatial, and a sub-period temporal resolution, reveal electric field lines, electric field vortices and saddle points. From our measurements we are able to reconstruct the magnetic field and, finally, the position and time-dependent Poynting vector which shows the flow of energy behind the sample. Our results show that it is possible to study the flow of light near sub-wavelength plasmonic structures such as slit-arrays and, by implication, other metamaterial samples.

OCIS codes: (180.0180) Microscopy; (260.3090) Far-infrared; (320.7160) Ultrafast technology.

References and links

1. J. C. Maxwell, *A Treatise on Electricity & Magnetism*, Third ed., (Oxford University Press, USA, 1891).
2. J. H. Poynting, "On the transfer of energy in the electromagnetic field," Philos. Trans. R. Soc. London **175**, 343-361 (1884).
3. D. R. Smith, J. B. Pendry, and M. C. K. Wiltshire, "Metamaterials and negative refractive index," Science **305**, 788-791 (2004).
4. D. Schurig, J. J. Mock, B. J. Justice, S. A. Cummer, J. B. Pendry, A. F. Starr, and D. R. Smith, "Metamaterial electromagnetic cloak at microwave frequencies," Science **314**, 977-980 (2006).
5. B. J. Justice, J. J. Mock, L. Guo, A. Degiron, D. Schurig, and D. R. Smith, "Spatial mapping of the internal and external electromagnetic fields of negative index metamaterials," Opt. Express **14**, 8694-8705 (2006).
6. A. P. Hibbins, M. J. Lockyear, I. R. Hooper, and J. R. Sambles, "Microwave transmission of a compound metal grating," Phys. Rev. Lett. **96**, 257402/1-4 (2006).
7. K. S. Yee, "Numerical solution of initial boundary value problems involving Maxwell's equations in Isotropic Media," IEEE Trans. Antennas Propag. **14**, 302-307 (1966).
8. G. Lévêque and O. J. F. Martin, "Optical interactions in a plasmonic particle coupled to a metallic film," Opt. Express **14**, 9971-9981 (2006).
9. K. Yang, L. P. B. Katehi, and J. F. Whitaker, "Electro-optic field mapping system utilizing external gallium arsenide probes," Appl. Phys. Lett. **77**, 486-488 (2006).
10. T. Pfeifer, H. –M. Heiliger, T. Loffler, C. Ohlhoff, C. Meyer, G. Lupke, H. G. Roskos, and H. Kurz, "Optoelectronic On-Chip Characterization of Ultrafast Electric Devices: Measurement Techniques and Applications," IEEE J. Quantum Electron. **2**, 586-604 (1996).
11. C. Genet and T. W. Ebbesen, "Light in tiny holes," Nature **445**, 39-46 (2007).
12. T. Matsui, A. Agrawal, A. Nahata, and Z. V. Vardeny, "Transmission resonances through aperiodic arrays of subwavelength apertures," Nature **446**, 517-521 (2007).
13. X. Shou, A. Agrawal, and A. Nahata, "Role of metal film thickness on the enhanced transmission properties of a periodic array apertures," Opt. Express **13**, 9834-9840 (2005).

14. F. Miyamaru, M. Tanaka, and M. Hangyo, "Effect of hole diameter on terahertz surface-wave excitation in metal-hole arrays," Phys. Rev. B **74**, 153416/1-4 (2006).
15. L. Martín-Moreno, F. J. García-Vidal, H. J. Lezec, K. M. Pellerin, T. Thio, J. B. Pendry, and T. W. Ebbesen, "Theory of Extraordinary Optical Transmission through Subwavelength Hole Arrays," Phys. Rev. Lett. **86**, 1114-1117 (2001).
16. M. van Exter and D. R. Grischkowsky, "Characterization of an optoelectronic terahertz beam system," IRE Trans. Microwave Theory and Tech. **38**, 1684-1691 (1990).
17. Q. Wu and X. C. Zhang, "Free-space electro-optic sampling of terahertz beams," Appl. Phys. Lett. **67**, 3523-3525 (1995).
18. G. Zhao, R. N. Schouten, N. van der Valk, W. T. Wenckebach, and P. C. M. Planken, "Design and performance of a THz emission and detection setup based on a semi-insulating GaAs emitter," Rev. Sci. Instrum. **73**, 1715-1719 (2002).
19. K. Wang and D. M. Mittleman, "Metal wires for terahertz wave guiding," Nature **432**, 376-379 (2004).
20. Tae-In Jeon, D. Grischkowsky, A. K. Mukherjee, and Reghu Menon, "Electrical characterization of conducting polypyrrole by THz time-domain spectroscopy," Appl. Phys. Lett. **77**, 2452-2454 (2000).
21. Seung Jae Oh, Chul Kang, Inhee Maeng, Joo-Hiuk Son, Nam Ki Cho, Jin Dong Song, Won Jun Choi, Woon-Jo Cho, and Jung Il Lee, "Measurement of carrier concentration captured by InAs/GaAs quantum dots using terahertz time-domain spectroscopy," Appl. Phys. Lett. **90**, 131906/1-3 (2007).
22. H. Caglayan, I. Bulu, and E. Ozbay, "Extraordinary grating-coupled microwave transmission through a subwavelength annular aperture," Opt. Express **13**, 1666-1671 (2005).
23. D. W. Pohl, W. Denk, and M. Lanz, "Optical stethoscopy : image recording with resolution lambda/20, " Appl. Phys. Lett. **44**, 651-653 (1984).
24. Q. Chen, Z. Jiang, G. X. Xu, and X. –C. Zhang, "Near-field terahertz imaging with a dynamic aperture," Opt. Lett. **25**, 1122-1124 (2000).
25. O. Mitrofanov, M. Lee, J. W. P. Hsu, L. N. Pfeiffer, K. W. West, J. D. Wynn, and J. F. Federici, "Terahertz pulse propagation through small apertures," Appl. Phys. Lett. **79**, 907-909 (2001).
26. N. C. J. van der Valk and P. C. M. Planken, "Electro-optic detection of subwavelength terahertz spot sizes in the near field of a metal tip," Appl. Phys. Lett. **81**, 1558-1560 (2002).
27. W. Zhu and A. Nahata, "Electric field vector characterization of terahertz surface plasmons," Opt. Express **15**, 5616-5624 (2007).
28. M. A. Seo, A. J. **L.** Adam, D. H. Kang, P. C. M. Planken, and D. S. Kim, in preparation (2007).
29. S. Keiding D. R. Grischowsky, M. van Exter, and Ch. Fattinger, "Far-Infrared Time-Domain Spectroscopy with Terahertz Deams of Dielectrics and Semiconductors," J. Opt. Soc. Am. B **7**, 2006-2013 (1990).
30. D. H. Auston, "Impulse response of photoconductors in transmission lines," IEEE J. Quantum Electron. **19**, 639-648 (1983).
31. Z. Jiang, M. Li, and X. C. Zhang, "Dielectric constant measurement of thin films by differential time domain spectroscopy," Appl. Phys. Lett. **76**, 3221-3223 (2000).
32. G. Gallot and D. R. Grischkowsky, "Electro-optic detection of terahertz radiation," J. Opt. Soc. Am. B **16**, 1204-1212 (1999).
33. D. F. Nelson and E. H. Turner, "Electro-optic and piezoelectric coefficients and refractive index of gallium phosphide," J. Appl. Phys. **39**, 3337-3343 (1968).
34. N. C. J. van der Valk, W. A. M. van der Marel, and P. C. M. Planken, "Terahertz polarization imaging," Opt. Lett. **30**, 2802-2804 (2005).
35. J. W. Lee, M. A. Seo, S. C. Jeoung, J. H. Kang, Q-Han Park, and D. S. Kim, "Fabry-Perot Effects in THz Time-domain Spectroscopy of Plasmonic Band-gap Structures," Appl. Phys. Lett. **88**, 071114/1-3 (2006).
36. A. P. Hibbins, B. R. Evans, and J. R. Sambles, "Experimental verification of designer surface plasmons," Science **308**, 670-672 (2005).
37. J. B. Pendry, L. Martin-Moreno, and F. J. Garcia-Vidal, "Mimicking surface plasmons with structured surfaces," Science **305**, 847-848 (2004).
38. K. G. Lee, H. W. Kihm, J. E. Kihm, W. J. Choi, H. Kim, C. Ropers, D. J. Park, Y. C. Yoon, S. B. Choi, D. H. Woo, J. Kim, B. Lee, Q. H. Park, C. Lienau and D. S. Kim, "Vector field microscopic imaging of light," Nat. Photon. **1**, 53-56 (2007).
39. J. D. Jackson, *Classical Electrodynamics* Third ed., (John Wiley & Sons, Inc., 1998).
40. A. Leitenstorfer, S. Hunsche, J. Shah, M. C. Nuss, and W. H. Knox, "Detectors and sources for ultrabroadband electro-optic sampling: Experiment and theory," Appl. Phys. Lett. **74**, 1516-1518 (1999).
41. M. L. M. Balistreri, H. Gersen, J. P. Korterik, L. Kuipers, and N. F. van Hulst, "Tracking Femtosecond Laser Pulses in Space and Time," Science **294**, 1080-1082 (2001).

1. Introduction

In Maxwell's electromagnetic theory of light [1], a point $\vec{x}$ in space is characterized by the time-dependent electric and magnetic field vectors $\vec{E}(\vec{x},t)$ and $\vec{H}(\vec{x},t)$ respectively. Poynting

[2] later derived his energy conservation theorem equating the energy flow $\vec{S}$ with the cross product of these two vectors: $\vec{S} = \vec{E}(\vec{x},t) \times \vec{H}(\vec{x},t)$. Advances in metamaterials research [3-6] demand precise knowledge on how these three vectors behave both in time and in space, since they all behave in a non-trivial manner near sub-wavelength structures. While the full electromagnetic field can be calculated with the highest degree of precision using such theoretical tools, such as the finite-difference-time-domain method [7], *experimentally* capturing the vectorial electrodynamics of light has remained a formidable challenge. In principle, one would like to plot the electric field, magnetic field, and Poynting vectors with subwavelength spatial resolution and sub-cycle temporal resolution in the broadest possible spectral range [8]. Such vector spatiotemporal microscopy would allow full-diagnostics of the metamaterial performance in time and space, which is essential for the realization of many proposed applications of these new classes of materials [3-5]. A pioneering work in the microwave range, using electro-optic crystals, measured all three electric field components [9]. Earlier, an electro-optic sampling techniques has been developed to measure fringing fields of high-frequency electrical circuits with a high spatial resolution [10], which can be extended to field mapping of all three components.

Increasingly, methods developed in the THz frequency range of the electromagnetic spectrum are applied to the study of, for example, the extraordinary transmission [11] of light through sub-wavelength arrays of holes in metal films or foils [12-15]. This is especially true for terahertz time-domain spectroscopy (THz-TDS), which is a spectroscopic technique capable of measuring the phase and amplitude of the electric field in an ultra-wide THz bandwidth [16-21]. This contrasts sharply with techniques developed for the visible and near-infrared region of the spectrum, which are typically based on intensity measurements in a relatively limited frequency range. An additional advantage of using THz light instead of visible light is that structure dimensions can be scaled up by a factor proportional to the THz-to-visible wavelength ratio, although it must be realized that this property is by no means unique to the THz frequency range [22]. Ideally, the effects of a structure on the electromagnetic field are most directly observed in the near-field of the structure. For a single, isolated, sub-wavelength-sized object, this is in fact the only way, since the diffraction limit implies that such an object will have little discernible effect on the far-field. For visible-, or near-IR light, near-field studies of small objects are typically performed using a sub-wavelength near-field detector, such as a tapered optical fiber [23]. More recently, near-field techniques have been reported, based on the use of dynamic apertures [24], static apertures [25], metal tips [26]. These methods, however, operate in a fairly narrow bandwidth, they typically measure intensity instead of field, and they don't allow a clear separation between the three orthogonal vector components of the electric field. We note that in a very recent paper, a measurement of the three vector components of the THz electric field at a single point was reported and the extent of the electric field into free space of a surface plasmon at this location was measured [27].

Here, we report on the development of a new type of near-field vectorial Fourier Transform *2D microscopy* [28] which fully utilizes the advantages of terahertz time domain spectroscopy (THz-TDS) [29-31]. Using a sample consisting of multiple sub-wavelength-sized slits in a metal foil, we show how we can measure the full electric field vector in an entire region of space behind the slits, with a sub-wavelength spatial resolution and a sub-period temporal resolution. From our measurements of the full electric field, we obtain the time-dependent *magnetic field* vectors, and finally the *Poynting* vectors in the same region of space. Together, these constitute and characterize the complete *electromagnetic field* near the slits, in the frequency range of 0.05 to 1.5 THz. The general applicability of our method may lead to an improved understanding of the flow of light near, for example, metamaterials.

2. Experiments and results

Figure 1(a) shows the schematics of our terahertz vector microscope. An *x*-polarized terahertz beam is incident upon a single slit sample with a slit width of $50\,\mu m$. Around the exit side of

the slit, electric field vectors have a strong positional dependence. Each of the vector components of the electric field $\vec{E}(x, 0, z, t) = [E_x(x, 0, z, t), 0, E_z(x, 0, z, t)]$ is detected using the electro-optic sampling technique [32] in which a THz electric field induces a refractive-index change in an electro-optic (EO) material at visible–near-IR frequencies that is proportional to the instantaneous field. This refractive-index change affects the ellipticity of a circularly polarized, synchronized, ultrashort probe laser pulse which is focused to a small spot less than 10 μm on the front surface of the EO-crystal, using a reflective objective. The probe pulse, reflected from the front surface, is sent to a standard differential detection setup which measures the ellipticity of the probe beam. By varying the time-delay between the probe pulse and the THz pulse, the full electric field as a function of time is obtained. Two different EO-crystals with a thickness of 300 μm are used. The vertical electric-field component E_z is detected using a (001) oriented GaP crystal, while E_x is detected using a (110) GaP crystal [33, 34]. The E_y component is measured by rotating the (110) crystal by 90 degrees but due to the incident polarization being along the x-axis, an E_y component is neither expected, nor measured. The crystals are initially in near-contact with the sample, with an air-gap of about 50 μm separating the crystals from the sample. The EO crystal is raster-scanned in the x-z-plane with a step size of 20 μm and at each pixel, the temporal evolution of the electric field is measured.
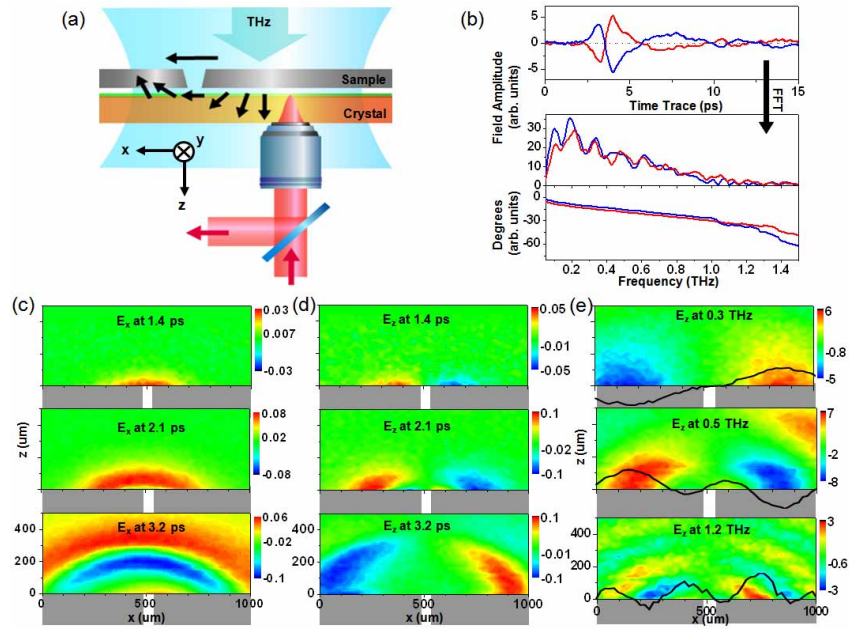

Fig. 1. (a). Schematic of the terahertz near-field microscopy setup. Electro-optic sampling is used to detect the real-time electric field at each position. We raster-scan the sample first to obtain data along the x-axis and then move the sample upward. We use two GaP crystals with their crystal orientation along the (110) and (001), respectively to detect the x- and z-components of the electric field. (b). The near-field E_z time-traces measured at two equal-distance points (red: left side; blue: right side) 400 μm away from the slit, along with their FFT spectra and phase. (c). E_x amplitudes at a fixed time, 1.4 ps, 2.1 ps, and 3.2 ps, respectively, when the bulk of the terahertz pulse has passed through the slit. An E_x movie for terahertz pulse emanating from a single slit in real time (2.458 MB) is shown. (d). E_z amplitude at a fixed time, 1.4 ps, 2.1 ps, and 3.2 ps. An E_z movie for terahertz pulse emanating from a single slit in real time (3.146 MB) is shown. (e). Fourier-transformed images at temporal phase $\omega t' = 0$, obtained from the movie captured in (c)., at the frequencies of 0.3 THz, 0.5 THz, and 1.2 THz. The black lines are E_z fields at z=0.

A Fast Fourier Transform (FFT) of the raster-scanned time traces at every pixel results in images at each frequency component at a zero temporal phase, $\omega t' = 0$ over the entire spectral range, complete with amplitude and phase:

$$\vec{E}(x, 0, z, \omega) = \frac{1}{2\pi} \int \vec{E}(x, 0, z, t') e^{i\omega t'} dt' \qquad (1)$$

The experimental image reconstruction based on Eq. (1) can plot the steady-state images at each frequency component from the time-domain signal. Two examples of time-traces for the THz near-field E_z component measured in this way are shown in Fig. 1(b). The blue line represents the trace with the microscopic objective positioned $400\,\mu m$ away from the right edge of the slit, while the red line represents a measurements obtained $400\,\mu m$ from the left edge of the slit. The two time traces show a phase difference of 180 degrees while their spectra, obtained by transforming the time traces, are practically identical (middle curves). The phase keeps increasing with increasing frequency, a clear indication that we are dealing with a propagating wave.

Figures 1(c) and 1(d) capture the out-going electric field profiles at three selected times, emphasizing the progression of the wave fronts, for both the E_x (c) and the E_z (d) components (see online supporting materials for more details). It is interesting to note that the E_z component is anti-symmetric while the E_x component is symmetric with respect to the slit axis. This difference originates from the normal-incident nature of the experimental geometry, with the incident polarization along the x-axis. Another point of interest is that exactly at the metal surface, the horizontal electric field E_x should be zero whereas it is non-zero in our experiments. This is easily explained by realizing that at $z=0$ we still have the air-gap between the EO-crystal and the sample, which implies that we measure the field a short distance away from the surface rather than exactly at the surface.

Generally, the maximum response of the (001) and (110) crystals to the THz electric field should be the same [33]. However, to allow for possible differences in the response of the crystals, we assume they are the same to within a scaling factor only. This scaling factor must be determined before the vector field can be plotted. Fortunately, we can use the property of light that in the far-field zone, away from the single slit [Figs. 1(c) and 1(d)], the electric field vector should be tangential to the wave-front. The scaling factor is simply adjusted until this condition is met.

Figure 1(e) shows such Fourier-transform microscope images for selected frequencies for the E_z component. As expected, with increasing frequency, the wave-fronts of the traveling waves become more closely spaced, which demonstrates that our novel concept works.

We also imaged the transmission through a multiple slit sample with a periodicity of $500\,\mu m$, where a far-field transmission spectrum shows an enhanced transmission [11] peak at about 0.5 THz [35]. The out-going time-traces at each position are again Fourier-transformed to generate images at each frequency. The image of E_x at 0.5 THz is dominated by an out-going traveling wave, distorted in the near-field by a smaller standing wave component [Fig. 2(a)], as can be seen by varying the temporal phase ωt from 0 to π, where $\vec{E}(x, 0, z, \omega, t) = \vec{E}(x, 0, z, \omega) \cdot e^{-i\omega t}$. In stark contrast, E_z is dominated by the evanescent standing wave components [Fig. 2(b)]. The surface-bound field can be thought of as the first order diffraction, which is evanescent because the frequency is below the Rayleigh minimum at 0.6 THz. Equivalently, it can also be viewed as the z-component of the *designer surface plasmon* electric field [36, 37]. At a larger frequency of 1 THz, the Fourier-transformed images are dominated by the interference between the 0th and 1st order diffractions, as can be explicitly visualized in Figs. 2(c) and 2(d). It is thus clear that any frequency component over the broad terahertz spectral range can be imaged with full information on amplitude and phase. We now show that we can use this information to construct vectorial images of the electromagnetic field through the multiple slit structure.
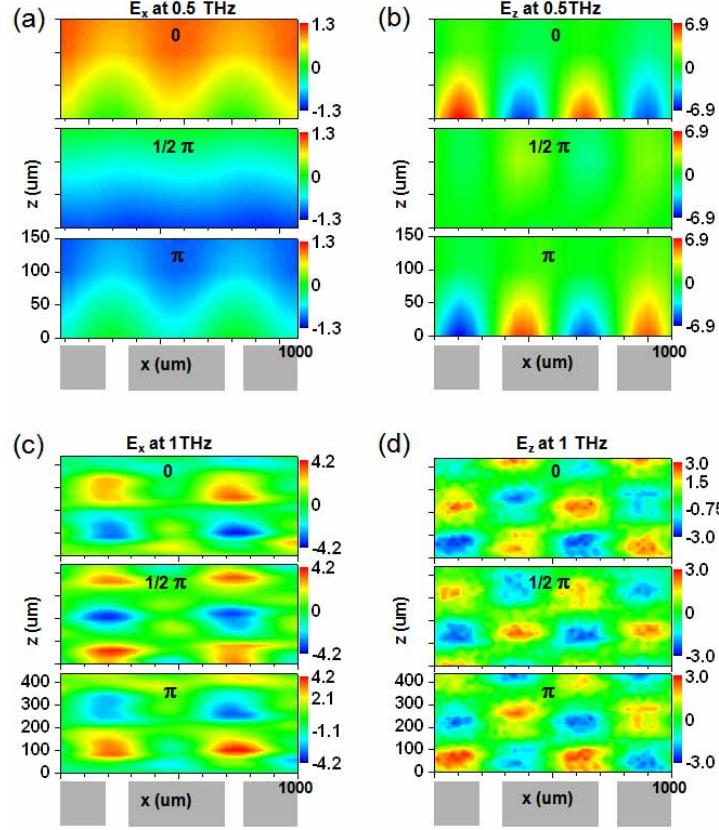
Fig. 2. (a). Fourier-transform E_x images at 0.5 THz at ωt =0, π /2, and π . (b) Same as (a) except that we now measure E_z. (c) Same as (A) except that the frequency is 1 THz. (d) Same as (b) except the frequency is 1 THz.

Figure 3 shows a Fourier-transformed steady state electric field vector image at 1 THz, fixing the temporal phase ωt at zero. At this frequency, the electric-field pattern is dominated by the interference between the 0th, and the $\pm 1^{st}$ order diffractions and two salient features are apparent: an electric field saddle point and an electric field vortex around a null electric field point. We can understand the saddle point and the vortex point in the following way. Around the null electric field point located at $(x_0, 0, z_0)$, both the vortex and the saddle point, with the forms $\vec{E}(x, 0, z, t) \propto (z-z_0, 0, -(x-x_0))e^{-i\omega t}$ and $\vec{E}(x, 0, z, t) \propto (x-x_0, 0, -(z-z_0))e^{-i\omega t}$, respectively, satisfy the divergence equation $\vec{\nabla} \cdot \vec{E} = 0$. However, these regions are expected to have different curls. Since we measure the field, rather than intensity, we can directly apply the Maxwell-Faraday equation:

$$\frac{\partial \vec{H}(x, 0, z, t)}{\partial t} = -c \cdot \vec{\nabla} \times \vec{E}(x, 0, z, t) \tag{2},$$

to obtain the magnetic field at each position. Taking the curl to access the magnetic field is possible because our THz-TDS setup provides information on both the amplitude and the phase of each electric field component. We note that direct measurements of the magnetic field are usually extremely difficult, but our measurements of the *full time-dependent electric field* make such measurements superfluous. At optical frequencies, it has recently been shown that it is possible to locally measure the polarization direction with 100 nm resolution [38] but without the phase information, it is impossible to deduce the magnetic field profile.
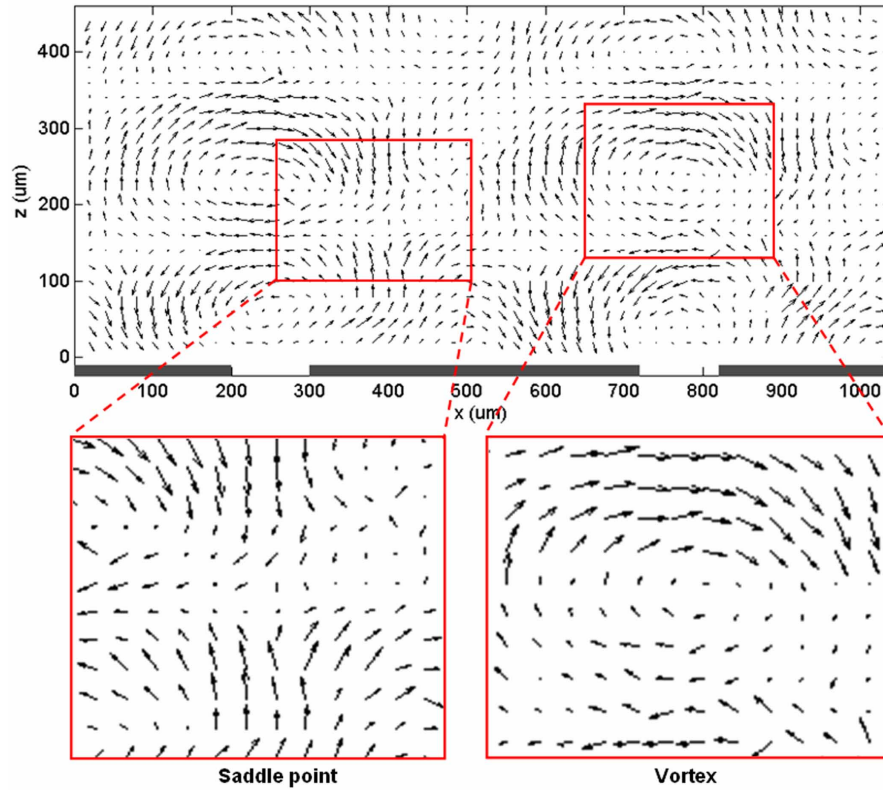
Fig. 3. Electric field vector mapping at 1 THz. An expanded view of the parts enclosed by the red-box regions can be seen in the lower part, showing saddle-point-like and vortex-like features. A Fourier-transformed electric field vector movie at 1 THz running the temporal phase, for light emanating from the multiple slit sample (3.026 MB) is shown.

By symmetry, we have only the y-component magnetic field, which is plotted in Fig. 4(a) together with the electric field vectors at the frequency of 1 THz. The experimentally obtained magnetic field profile, while noisy due to errors introduced when taking the derivative, reveals interference between the 0th and the $\pm 1^{st}$ diffraction orders. Now that we have the electric and magnetic field vectors at each position and in time, we can experimentally obtain the Poynting vector $\vec{S} = \vec{E} \times \vec{H}$ [39]. Our method provides a more direct measurement of power flow at each position, at a time, than the single component measurement recently performed in the microwave region [4].

In Fig. 4(b), the Poynting vector at 1 THz at a temporal phase, $\omega t' = 0$ is plotted. The experimental Poynting vectors $\vec{S}$ show complicated energy flow at this frequency, as clearly, $\vec{\nabla} \cdot \vec{S}$ is generally non-zero in Fig. 4(b). Non-zero divergence can be understood in connection with the changing local electromagnetic energy since the continuity equation must hold: $\vec{\nabla} \cdot \vec{S} + \dfrac{\partial u}{\partial t} = 0$, where u is the electromagnetic energy density [2]. The time-dependent movies for $\vec{S}$, are in good agreement with the FDTD theory, as shown in the supporting material movie. The Poynting vector images are a sensitive function of both the frequency and time, which we can access in the full broad terahertz frequency range through our Fourier-transform imaging method.
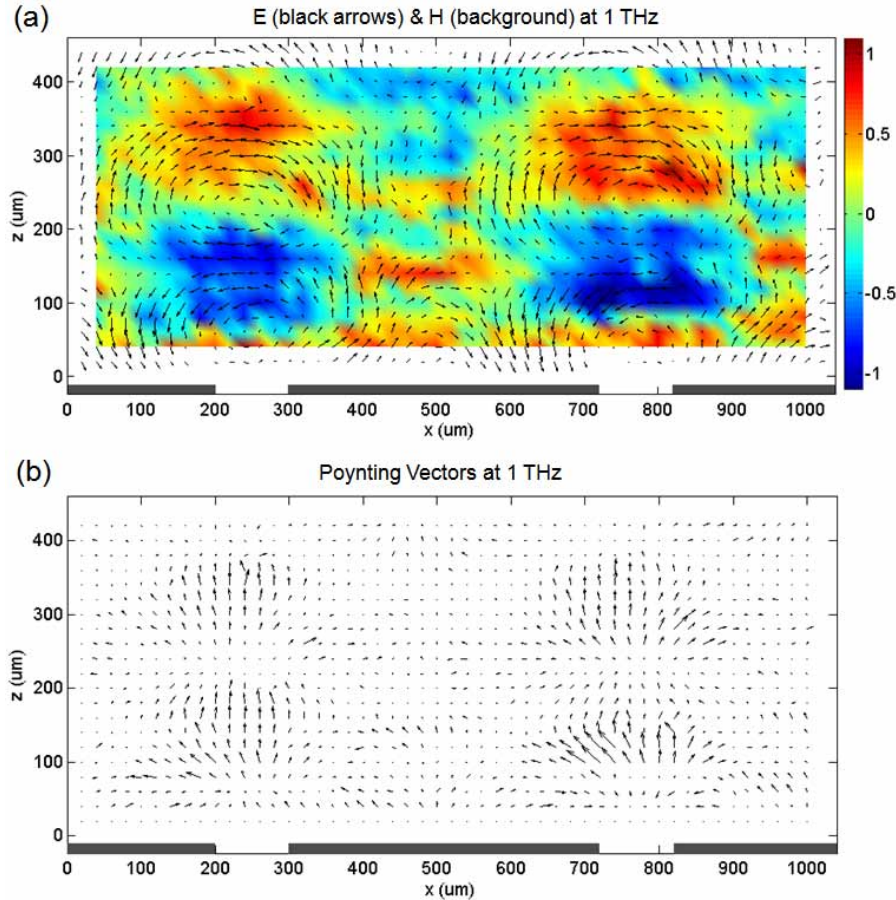
Fig. 4. (a). Magnetic field profile at 1 THz plotted together with the electric field vectors. A movie at 1 THz running the temporal phase, for light emanating from the multiple slit sample is shown (3.527 MB). The black line denotes the electric field and the background color represents the magnetic field. (b). Poynting vectors at 1 THz calculated from the results shown in (a). A Poynting vector movie at 1 THz running the temporal phase, for light emanating from the multiple slit sample (1.551 MB) is shown.

The time-averaged Poynting vectors at 1 THz, both from the experiment Fig. 5(a) and from the calculations Fig. 5(b), are plotted. The time-averaged Poynting vector images at 1 THz are concentrated around the slit axes, even as we move away from the near-field zone, suggesting that the propagating diffraction orders 0, +1 and -1 generate Poynting vector images that confirm to our macroscopic intuition. While the theory is largely consistent with experiment, there exists a modulation along the z-axis in the experimental data, which is absent in the theory. This is most likely due to etalon (or waveguide) effects between the sample and the crystal. The modulation period is approximately half the wavelength but this modulation is largely absent in the original (before taking the Fourier-transform), pulsed data, because in the time-domain data, all frequency components contribute and the waveguide effect averages out. That our Fourier-transformed, time averaged Poynting vector plots show these etalon effects, again demonstrates the validity and sensitivity of our technique.

(a)
Time-averaged Poynting Vectors at 1 THz

(b)
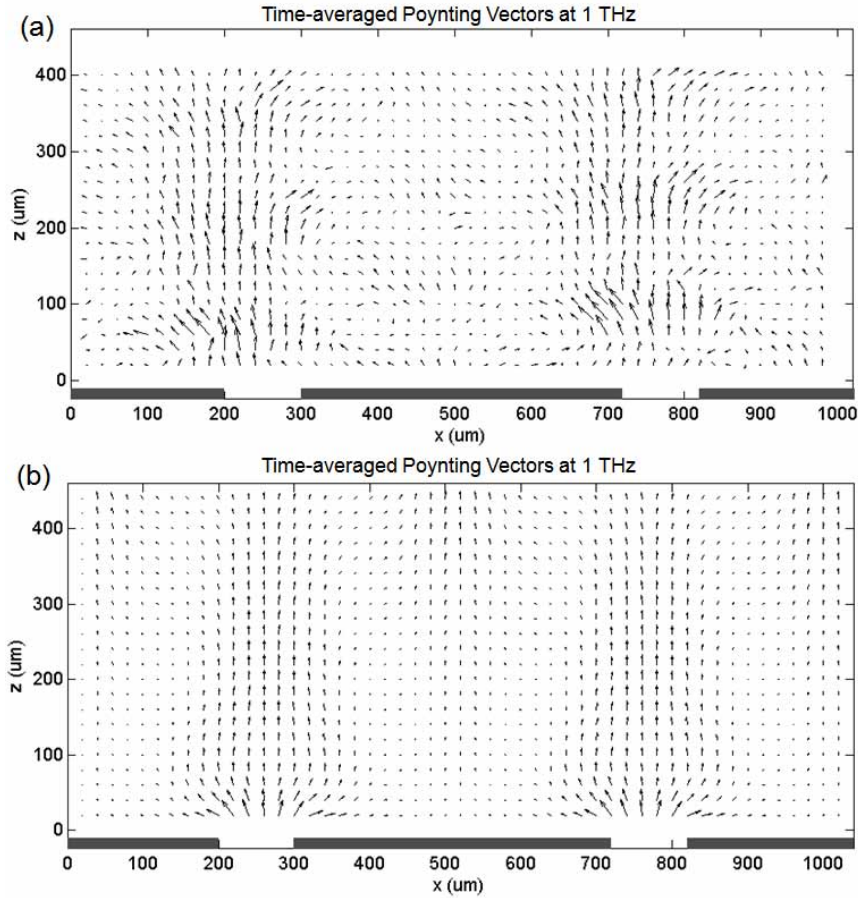**Time-averaged Poynting Vectors at 1 THz**

Fig. 5. (a). Time-averaged 2D Poynting vector behind the multiple slit sample at 1 THz, obtained from the 2D electric field vectors measured in the x-z-plane behind the slit sample and from the corresponding magnetic field vectors calculated from the electric field data. (b) FDTD simulation for time-averaged Poynting vector from the multiple slit sample, also at 1 THz.

3. Conclusion

In conclusion, our vector microscope accesses $\vec{E}(x,t)$, $\vec{H}(x,t)$, and $\vec{S}(x,t)$ experimentally in the broad frequency range between 0.05 and 1.5 THz. We expect that the vectorial Fourier-transform microscopy will be an invaluable imaging tool that visualizes electric field, magnetic field, and Poynting vectors around metamaterials. Considering that THz-TDS techniques, operating up to 70 THz [40] have been demonstrated, we expect that our approach can be extended to the mid-infrared. The results of our measurements are directly relevant to other frequency domains, such as the visible and microwave regimes [4, 41].

Acknowledgments